High performance single emitter homojunction interfacial work function far infrared detectors

D. G. Esaev, M. B. M. Rinzan, S. G. Matsik, and A. G. U. Perera[a)]
Department of Physics and Astronomy, Georgia State University, Atlanta, Georgia 30303

H. C. Liu
Institute for Microstructural Sciences, National Research Council, Ottawa K1A 0R6, Canada

B. N. Zvonkov and V. I. Gavrilenko
Institute for Physics of Microstructures, Nizhny Novgorod, Russia

A. A. Belyanin
Department of Physics, Texas A&M University, College Station, Texas 77843

(Received 28 May 2003; accepted 20 October 2003)

Results are reported on p-GaAs homojunction interfacial work function internal photoemission far infrared (HIWIP FIR) detectors with a $\sim 10^{19}$ cm^{-3} carbon doped single emitter and a barrier layer for three different barrier thicknesses. A remarkably high quantum efficiency with low dark current and an increased responsivity were observed for devices with 1-, 0.1-, and 4-μm-thick barrier regions. The dark current densities for these structures are on the order of $1-10$ μA/cm^2 at 4.2 K, corresponding to a high dynamic resistance compared with previous HIWIP FIR detectors. A detector with a barrier thickness of 1 μm had a peak responsivity of 18.6 A/W, a peak detectivity $D^*=9\times10^{11}$ cm$\sqrt{\text{Hz}}$/W, and a quantum efficiency of 40% at a wavelength of 58 μm under a reverse bias measured at 4.2 K. Cutoff wavelengths of these detectors vary with bias and are around 70 μm as expected. The main features of the absorption and responsivity spectra are well described based on a model incorporating free carrier absorption, hot hole transport, and emission over the barrier. © *2004 American Institute of Physics.* [DOI: 10.1063/1.1632553]

I. INTRODUCTION

Single element high performance far-infrared (40–200 μm) semiconductor detectors and large focal plane arrays are used for space astronomy applications, such as NASAs Space Infrared Telescope Facility program.[1] Present far infrared (FIR) detectors in use or under development for this wavelength range are extrinsic Ge photoconductors (stressed or unstressed),[2] and Ge[3] and Si[4] blocked-impurity-band (BIB) detectors. There are many technological challenges for fabricating Ge large format arrays, and GaAs BIB detectors are still in the developmental stages.

The basic structure of the homojunction interfacial work function internal photoemission (HIWIP) detector[5] consists of a heavily doped emitter layer and a barrier layer which is sandwiched between the conducting layers. For p-type structures the interfacial work function, Δ, is the offset between the Fermi level of the emitter and the valence band edge of the barrier, which arises due to the band gap narrowing of highly doped emitter layer. The detection mechanism involves free hole absorption in the emitter layer, followed by the internal emission of photoexcited carriers across the junction barrier. These photoemitted carriers are swept out of the active region by the electric field and are collected at the contact. Initially it was believed that, in principle, GaAs FIR detectors could be designed with arbitrarily long cutoff wavelength $[\lambda_c\ (\mu\text{m})=1.24/\Delta\ (\text{eV})]$,[6] since Δ can be made arbitrarily small with increased doping concentrations due to metal–insulator (Mott) transition.[7] As shown previously the λ_c was tunable from 76 to 85 μm by varying the Be doped emitter layer concentration from 1×10^{18} to 3×10^{18} cm^{-3}.[8] However, in practice the heavy-hole to light-hole transition in the valence band of highly doped emitter region limits the λ_c value to ~100 μm.[9] Here, carbon doped GaAs HIWIP FIR detectors with different barrier thicknesses, having a λ_c around 70 μm with high quantum efficiencies are reported.

II. EXPERIMENT

The HIWIP samples were grown by the metalorganic chemical vapor deposition technique at 610 °C on a semi-insulating GaAs (100) substrate. The structures consist of a bottom contact (p^{++}) layer, a barrier layer, an emitter (p^{+}) layer, and a top contact layer as shown in Fig. 1. Three single emitter layer structures (RU001, RU002, and RU003) with carbon as the dopant were processed. The layer parameters (thickness and doping level) of the samples shown in Table I were confirmed by secondary ion mass spectroscopy (SIMS). Mesas with different optical window areas were processed for responsivity characterization. The top contact and a part of the emitter layer were etched out, leaving about 800-Å-thick emitter regions in each sample.

The p-GaAs HIWIP FIR detectors were characterized by I–V and responsivity measurements. Here, forward bias refers to a positive voltage on the top contact while the reverse bias refers to a positive voltage on the bottom contact. Trans-

a)Electronic mail: uperera@gsu.edu

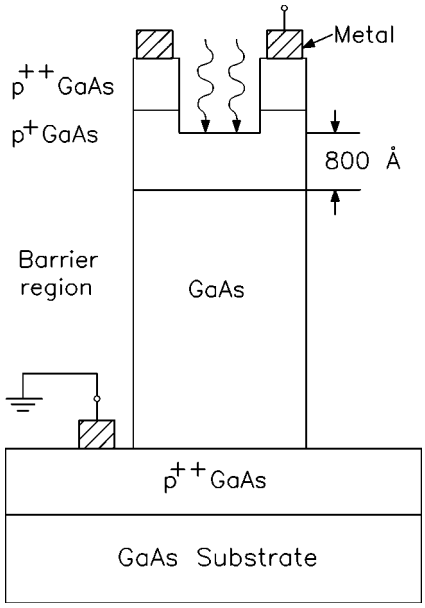

FIG. 1. Schematic of the p-GaAs single emitter HIWIP detector after processing. p^{++}, p^{+}, and barrier are the contact layer, emitter layer, and barrier layer, respectively. A window is opened on the top for frontside illumination. The three structures RU001, RU002, and RU003 have 4-, 0.1-, and 1-μm-thick barrier region, respectively.

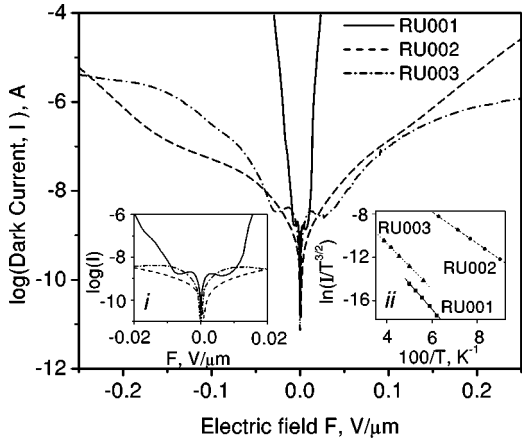

FIG. 2. Dark current curves for the three structures at 4.2 K. The asymmetry in the dark current curves is due to nonuniformity in the structures. The rapid rise of dark current in RU001 can be attributed to defects in the barrier. Inset (i) shows the dark current behavior in enlarged scale. Inset (ii) shows the Arrhenius plots under the forward electric fields 0.005, 0.3, and 0.1 V/μm for samples RU001, RU002, and RU003, respectively.

mission and reflection measurements were performed with a resolution of 4 cm^{-1} for unetched samples using a Perkin–Elmer system 2000 Fourier-transform infrared spectrometer with a Si composite bolometer as the reference. Transmission was measured at normal incidence, and reflection at an incidence angle of around 8°. Absorption spectra were obtained as the difference between unity and the sum of the reflection and transmission spectra.[10]

III. RESULTS AND DISCUSSION

The dark current for the detectors at 4.2 K is shown in Fig. 2. Inset (i) shows the dark current in the narrow range of the electric field from -0.02 to 0.02 V/μm. The sharp increase in the dark current for RU001 at an electric field of $\sim$0.01 V/μm could be attributed to tunneling associated with the material defects.[11] Defect formation increases for thicker layers even for low defect materials such as GaAs.[12] However, the dark current in the bias region of operation is still low and the overall performance of the detectors is not affected.

The Arrhenius plots for determining the barrier heights under the forward electric fields of 0.005, 0.3, and 0.1 V/μm for samples RU001, RU002, and RU003, respectively, are shown in the inset (ii) in Fig. 2. The forward bias Arrhenius plot for RU002 indicates a barrier height of 14 meV while the reverse gives a barrier height of 17 meV, by extrapolating the experimental data to zero electric field. For samples RU001 and RU003 no difference was observed in the barrier height for forward and reverse bias. As seen from Table I, the difference between the doping concentration of the emitter (0.5×10^{19} cm^{-3}) and the bottom contact (3×10^{19} cm^{-3}) is largest for sample RU002, which produces a built-in electric field in the barrier that was estimated to be about 0.2 V/μm. The barrier lowering due to this internal field is about 5 meV at the emitter-barrier interface. This barrier lowering and the band gap narrowing, according to the high density theory,[5] will form different barriers for the forward and reverse bias cases.

The electric field dependence of the effective barrier height for the three samples under forward bias is shown in Fig. 3. Sample RU001 has a sharp drop in barrier height at a field strength of 0.01 V/μm limiting the operating field, which is directly related to the increasing dark current discussed before. Samples RU002 and RU003 also show slow barrier lowering with increasing field due to the image force lowering,[5] and their λ_c is expected to vary with the bias voltage.

Room temperature experimental and calculated absorption spectra for unetched pieces from the same wafers as the detector samples RU001, RU002, and RU003 are shown in Fig. 4. The calculations were based on Drude model for the

TABLE I. Main parameters for the three device structures as grown, and confirmed by SIMS measurements. Here, N_{tc} (W_{tc}), N_{em} (W_{em}), N_b (W_b), and N_{bc} (W_{bc}) are the doping concentration (thickness) of the top contact, emitter, barrier, and bottom contact of the single emitter structure, respectively.

Sample	W_{tc} (nm)	N_{tc} 10^{19} cm^{-3}	W_{em} (nm)	N_{em} 10^{19} cm^{-3}	W_b (μm)	N_b 10^{17} cm^{-3}	W_{bc} (μm)	N_{bc} 10^{19} cm^{-3}
RU001	120	5.9	200	1.6	4.0	2	1	3.0
RU002	150	5.0	200	0.5	0.1	3.0	1	3.0
RU003	120	5.3	200	1.5	1.0	1.8	1	2.0

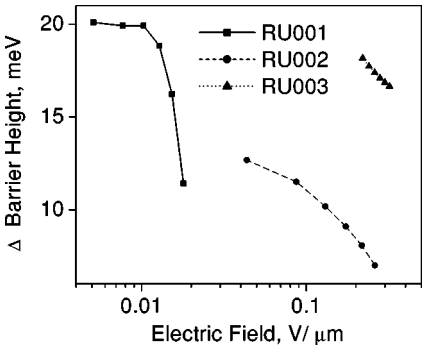

FIG. 3. The change in the effective barrier height as the forward electric field varies in the structures at temperature 4.2 K. The sample with 4-μm-thick barrier region has an almost constant barrier up to 0.01 V/μm and then decreasing sharply, whereas the other two samples show expected behavior of bias variation due to the image force lowering. This increases the dark current in RU001 sharply as compared to the samples RU002 and RU003 with 0.1- and 1-μm-thick barrier regions as shown in Fig. 2.

interaction of radiation with free carriers and optical phonons in the frame of Lorenz model.[13] A two component free-carrier plasma consisting of heavy holes (HH) and light holes (LH) was considered. Although the light hole is only about 5% of the total concentration, the high mass ratio (7:1) of HH:LH causes the plasma frequencies for both carriers to be of the same order.[14] Details of the model and calculation of the optical electric field distribution across the structure, and reflection/transmision calculations of the structure were described in Ref. 15. Thickness and doping level for the structures were obtained by fitting the calculated transmission and reflection spectra to the experimental results. These values are within 5% of the design parameters.

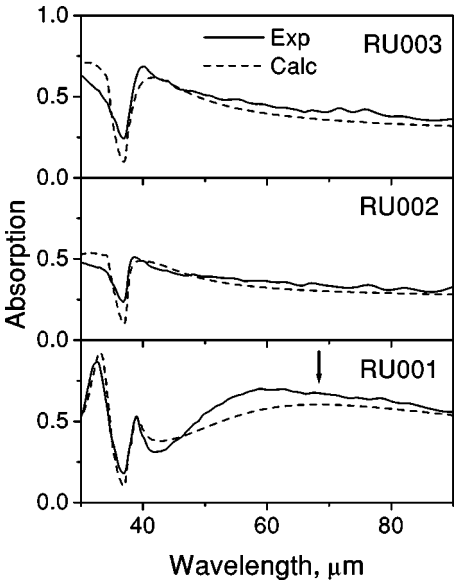

FIG. 4. The experimental (solid line) and calculated (dashed line) absorption spectra at room temperature for the samples with different barrier thickness. The absorption measurements were done for pieces without top-contact etching. RU001 has a 4-μm-thick barrier region and the others, RU002 and RU003, have 0.1- and 1-μm-thick barriers, respectively. The first order cavity peak for structure RU001 is around 68 μm, and is marked by an arrow. Higher order peaks for sample RU001 and peaks of all orders for samples RU002 and RU003 are outside the range of measurements.

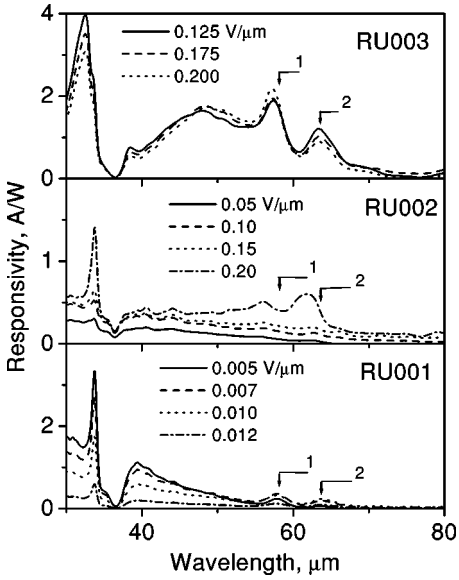

FIG. 5. The experimental responsivity spectra for detectors at 4.2 K under different forward electric fields. Maximum responsivity is at 34 μm, and its value are 3.3, 1.4, and 4 A/W for detectors RU001, RU002, and RU003, respectively. The first order cavity peak for detector RU001 is around the cutoff wavelength. The sharp drop around 37 μm is due to the high reflection in the reststrahlen band. Arrows 1 and 2 indicate the transitions between the ground and the excited impurity (carbon) states. Arrow 1—transition $1S_{3/2}(\Gamma_8)\rightarrow 2P_{5/2}(\Gamma_7)$, arrow 2—transition $1S_{3/2}(\Gamma_8)\rightarrow 2P_{5/2}(\Gamma_8)$ (see Ref. 16).

Resonant cavity enhancement,[10] attributed to the Fabry–Pérot interference, is expected in these structures due to reflection from highly doped emitter and bottom contact layers. The resonance wavelength can be estimated by the expression

$$\sum_j \mathrm{Re}[n_j(\lambda)]d_j=(\lambda/4)(2m-1),\quad m=1,2,3\ldots, \qquad (1)$$

where $\mathrm{Re}(n_j)$ is the real component of the refractive index of the jth layer, d_j is the thickness, and the summation is carried throughout the layers in the structure.

For sample RU001, taking the total thickness of the structures and the mean refractive index into account, the first ($m=1$) and second ($m=2$) order absorption peaks were calculated to be at 68 and 23 μm, respectively. The first order resonance absorption peak at 68 μm can be seen (indicated by arrow) in Fig. 4. The second order peak for RU001 and the first order peak for samples RU002 and RU003 (about 14.5 and 26 μm, respectively) are outside the measured spectral range. The sharp drop at 37 μm is due to high reflection at the reststrahlen band from GaAs caused by the strong photon-optical phonon interaction.

Strong bias dependence of the experimental responsivity for three structures is shown in Figs. 5 and 6. Maximum responsivity is achieved at electric fields of 0.005, 0.2, and 0.125 V/μm for forward bias and at 0.012, 0.2, and 0.25 V/μm for reverse bias for samples RU001, RU002, and RU003, respectively. As expected from the dark current behavior, the performance of sample RU001 degrades as the field approaches 0.01 V/μm, which was attributed to the high defect density in the barrier region. A resonance cavity peak

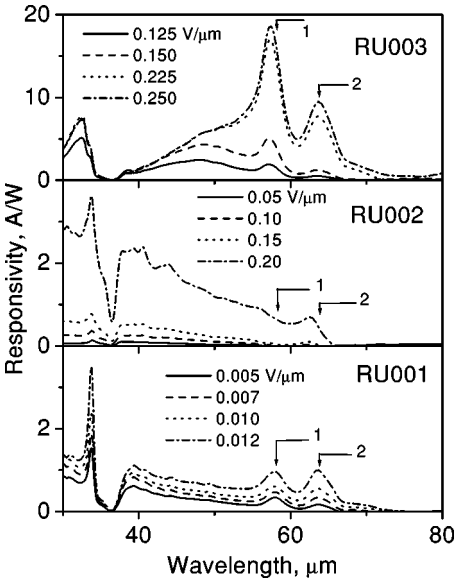

FIG. 6. The experimental responsivity spectra for detectors at 4.2 K under different reverse electric fields. Maximum responsivity is at 34 μm, and its value are 3.5, 3.6, and 7.4 A/W for detectors RU001, RU002, and RU003, respectively. The first order cavity peak for detector RU001 is around the cutoff wavelength. The sharp drop around 37 μm is due to the high reflection in the reststrahlen band. Arrows 1 and 2 indicate the transitions between the ground and the excited impurity (carbon) states. Arrow 1—transition $1S_{3/2}(\Gamma_8)\rightarrow 2P_{5/2}(\Gamma_7)$, arrow $2-1S_{3/2}(\Gamma_8)\rightarrow 2P_{5/2}(\Gamma_8)$ (see Ref. 16). High responsivity at 58 μm for sample RU003 is due to higher electric field and higher probability of the transition from the ground to the excited state.

was observed around 68 μm in the absorption spectum of sample RU001 presented in Fig. 4. However, this was not observed in the responsivity spectra due to photoemission drop around the λ_c of 70 μm.

Detector RU001 has a peak responsivity (at 34 μm) of 3.3 A/W and 3.5 A/W, $D^*=1.6\times10^{11}$ and 1.7×10^{11} cm$\sqrt{\text{Hz}}$/W, and quantum efficiency 12% and 12.8% for forward (0.005 V/μm) and reverse (0.012 V/μm) bias, respectively. Even though this sample has a 4-μm-thick barrier region, the 1-μm-thick bottom contact compared to an 800-Å-thick emitter layer maintains a high carrier generation rate in the bottom contact. This leads to the same order of responsivity observed for both bias directions. This detector can be used as a wide band detector in the range 40–65 μm with an average responsivity of 0.7 A/W.

The responsivity for the structure with 1 μm barrier region (RU003) has a strong bias dependence, increasing significantly with the bias. However, the bias cannot increase indefinitely as the dark current also increases with bias. At 34 μm, it has a peak responsivity of 7.4 A/W (4 A/W) giving a quantum efficiency of 27.2% (14.7%) and a detectivity D^* of 3.6×10^{11} cm$\sqrt{\text{Hz}}$/W (1.9×10^{11} cm$\sqrt{\text{Hz}}$/W) for 0.15 V/μm reverse (0.125 V/μm forward) bias. This detector shows a broad spectrum with an average responsivity of 3 A/W in the range 40–60 μm.

Responsivity peaks were observed, for forward and reverse bias spectra, at wavelengths 57 and 63 μm for all samples. They can be attributed to the hole transitions from the ground state to the excited impurity states in the relatively low-doped barrier layers. It has been shown, from the photoconductivity measurements, that the wavelength corresponding to transitions from the ground to the third excited impurity state $[1S_{3/2}(\Gamma_8)\rightarrow 2P_{5/2}(\Gamma_7)]$ is 58.2 μm and from the ground to the second excited state $[1S_{3/2}(\Gamma_8)\rightarrow 2P_{5/2}(\Gamma_8)]$ is 63.9 μm.[16] The degenerate excited state $2P_{5/2}$ splits into two states, $2P_{5/2}(\Gamma_7)$ and $2P_{5/2}(\Gamma_8)$, under the ''spin-orbit'' interaction in accordance with the point group symmetry in the zinc-blende structure of GaAs, that are denoted by the notations (Γ_7) and (Γ_8).[17] The wavelength corresponding to the transition from the ground state to the first excited state is 81 μm and lies outside the λ_c.

At low temperatures T, the carriers have insufficient thermal energy (kT, where k is the Boltzmann's constant) to occupy the excited states; hence, the ground state is mostly occupied. The enhancement of the photocurrent at these wavelengths is due to the transitions from the ground to the excited states and subsequent tunneling in the valence band through the barrier formed by the Coulomb potential of the acceptor and the external electric field. The last transition has a strong dependence on the electric field. As seen in Figs. 5 and 6, the strongest transitions were observed at the highest field. The small deviation in the peaks for sample RU002 and RU003 may be due to the Stark shift of the impurity levels caused by high electric field.

Increased responsivity in the 40–50 μm region due to transitions from the ground to the valence band is shown in Figs. 5 and 6. In accordance with Ref. 16 the ground state of the impurity lies at 26.9 meV above the valence band; therefore, the transition from the impurity ground to the valence band states would be expected around 46 μm. Transitions from the ground state to higher excited states ($1S\rightarrow 3P$) and from the ground state to continuum, in the range 40–50 μm, have also been observed.[16] They are more pronounced at low temperatures due to increased probability of ground-state occupation.

Peak responsivity, quantum efficiency, and detectivity of single emitter samples RU001, RU002, and RU003 are compared with another sample 9604 having 20 periods of emitter/barrier structure (total thickness of the emitters is 0.3 μm), reported previously,[18] as shown in Table II. Even though all three present detectors are single emitter structures, the responsivity is much greater than the multilayer structures that have been previously demonstrated.[19] These detectors have a λ_c of about 65–70 μm, which agrees with the interfacial work function calculated from the Arrhenius plots.

The main parameters of the detectors (responsivity, quantum efficiency, and detectivity) at wavelengths corresponding to transitions from the ground to excited impurity states are presented in Table III, indicating the highest responsivity for sample RU003. The low responsivity in RU001 is due to the high density of defects present in the structure preventing the operation at comparable electric fields. Sample RU002 has the lowest number of impurities due to its thin barrier region. As a result, it has the lowest responsivity.

The energy of plasma oscillations for the 5×10^{18} cm^{-3} doped emitter layer of sample RU002 is $\hbar\omega=33.6$ meV, while the optical phonon energies are $\hbar\omega_{\text{TO}}$

TABLE II. Figures of merit (peak responsivity, quantum efficiency, and detectivity) for the single emitter detectors RU001, RU002, and RU003 at 34 μm compared to the multiemitter detector 9604. The thickness of the emitter (800 Å) and the bottom contact (1 μm) for all three single emitter detectors are the same. Detector 9604 has 20 periods of emitter/barier structures (total thickness of the emitters is 0.3 μm) and the peak responsivity is at 34 μm (see Ref. 18).

Sample No.	Peak responsivity (A/W)		Quant. efficiency (%)		Detectivity $10^{11}\times$ cm$\sqrt{\text{Hz}}$/W	
	Forward	Reverse	Forward	Reverse	Forward	Reverse
RU001	3.3	3.5	12	12.8	1.6	1.7
RU002	1.4	3.6	5	13.3	0.7	1.7
RU003	4	7.4	14.7	27.2	1.9	3.6
9604	3.1	⋯	12.5	⋯	0.5	⋯

$=33.2$ meV and $\hbar\omega_{\text{LO}}=36.1$ meV. This produces a strong coupling between plasma oscillations and polar lattice vibrations giving rise to a plasmon with high damping, renormalizing the plasmon frequency,[20] and changing the free carrier absorption mechanism. The energy of plasma frequencies for samples RU001 and RU003 are 60.2 and 58.3 meV, respectively, shows the difference between the plasma and phonon frequencies for these samples is greater than for RU002, producing a weak phonon-plasmon coupling.

The responsivity calculations were performed by considering photoexcitation of holes in the emitter, photoemission, and hot-hole transport. Total quantum efficiency is the product of photon absorption, internal photoemission, and hot-hole transport probabilities, $\eta=\eta_a\eta_i\eta_t$. Responsivity at wavelength λ is given by

$$R=\eta\frac{q}{hc}\lambda, \tag{2}$$

where q is the electron charge, c is the speed of light in vacuum, and h is Planck's constant. The quantum efficiency of the internal photoemission η_i and hot-hole transport η_t were calculated using the model described before.[5]

The photon absorption probability η_a is defined as the fraction of the incident light that is absorbed by the free holes in the emitter and is calculated from the expression

$$\eta_a=2\frac{\omega}{c}\text{Im}[\varepsilon(\omega)]\frac{1}{|E_0|^2}\int_0^W|E(x)|^2dx$$
$$=2\frac{\omega}{c}\text{Im}[\varepsilon(\omega)]\frac{\overline{|E|^2}}{|E_0|^2}W, \tag{3}$$

where $\text{Im}[\varepsilon(\omega)]$ is the imaginary part of the dielectric constant, ω is the frequency, $\omega/c=2\pi/\lambda$ is the wave number of the incident light, E is the electric field of the electromagnetic wave inside the layer, E_0 is the electric field of the incident radiation, and W is the thickness of the emitter layer. The dielectric constant $\varepsilon(\omega)$ has two additive parts describing the light interaction with the free carriers and optical phonons. In Eq. (3) only the energy dissipation of the incident radiation by the free carriers is included, since only the photoexcited carriers contribute to photocurrent. Energy dissipated by phonon generation goes into the crystal lattice. The value of η_a is proportional to the mean square of the optical electric field in the structure. A calculation of the electric field distribution across the structure was carried out taking both the free carrier and optical phonon contributions to the permittivity into account. Formation of the standing waves in a structure has been discussed in detail before.[15]

The calculated and experimental spectral response measured at 4.2 K under forward and reverse bias are shown in Figs. 7 and 8, respectively. Since the model does not include

TABLE III. Figures of merit (peak responsivity, quantum efficiency, and detectivity) for the single emitter detectors RU001, RU002, and RU003 at wavelengths 58 and 64 μm, corresponding to transitions from the ground to the third and from the ground to the second excited states of the impurity (carbon), respectively. The maximum responsivity is achieved for the sample RU003, whereas high density of defects would not allow the electric field to be increased significantly for the sample RU001, and sample RU002 has the lowest barrier thickness resulting in the lowest number of the impurities.

Sample No.	Peak responsivity (A/W)				Quant. efficiency (%)				Detectivity $10^{11}\times$ cm$\sqrt{\text{Hz}}$/W			
	Forward μm		Reverse μm		Forward μm		Reverse μm		Forward μm		Reverse μm	
	58	64	58	64	58	64	58	64	58	64	58	64
RU001	0.33	0.23	0.96	1.0	0.7	0.4	2.1	1.9	0.16	0.11	0.47	0.49
RU002	0.51	0.6	0.91	0.70	1.1	1.2	2.0	1.4	0.25	0.29	0.44	0.34
RU003	2.18	1.21	18.6	9.51	4.7	2.4	40.0	18.6	1.06	0.59	9.04	4.62

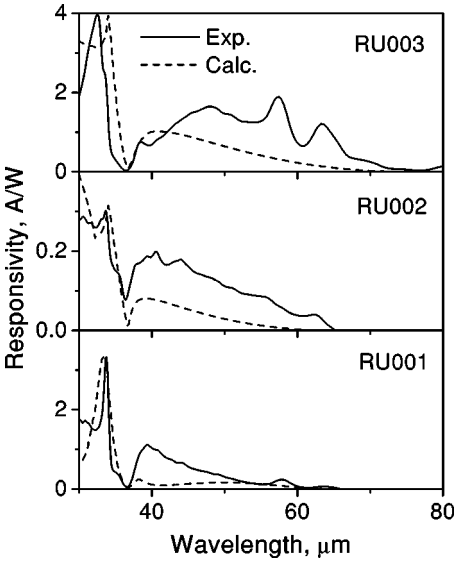

FIG. 7. Variation in responsivity with wavelength under forward bias at 4.2 K. Solid lines—experimental curves, dashed lines—calculated curves. The matching is done at electric fields 0.005, 0.05, and 0.15 V/μm for samples RU001, RU002, and RU003, respectively. Responsivity dip at 37 μm is due to high reflection in the reststrahlen band.

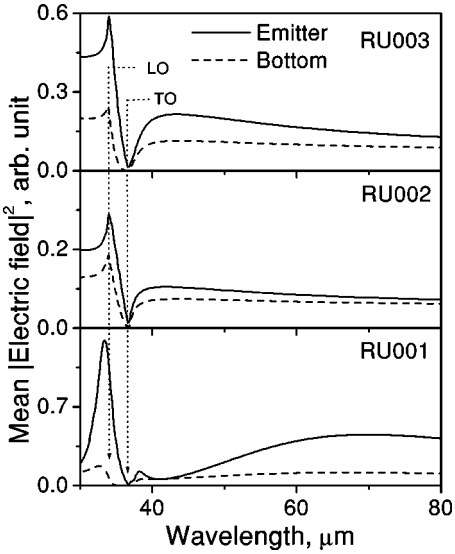

FIG. 9. Calculated mean square of optical electric field across the emitter and bottom contact layers of the three samples. The lowest electric field produced the lowest responsivity for sample RU002. Sharp drop at TO phonon frequency (36.7 μm) is due to the sharp increase of the permittivity in the vicinity. The peak electric field at LO phonon frequency (33.9 μm) is due to the dropping of permittivity to zero. The drop and rise of electric field result in the drop and rise of the responsivity as in the Figs. 5 and 6.

any electric field effects, the comparison with calculations was done for the low-bias experimental results. The calculations were carried out using the structure parameters (thicknesses and doping concentration) obtained by fitting the experimental reflection/transmission spectra to the calculated spectra. The emitter layer was 800 Å, which was the thickness remaining after the etching process. A reasonable agreement between experimental and calculated curves is observed in Figs. 7 and 8. The peak at 34 μm and the sharp drop at 37 μm are due to the interaction of radiation with LO and TO optical phonons and the variation of the optical electric field in the emitter and bottom contact as discussed later. The peaks at 58 and 64 μm, and the increased responsivity in the 40–50 μm spectral range in the experimental curves are due to transitions from the ground to the excited states of the impurity and from the ground to the valence band that were not included in the theoretical model.

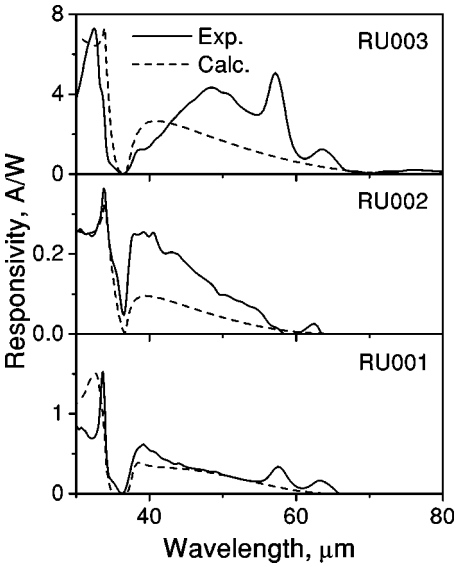

FIG. 8. Responsivity vs wavelength under the reverse bias at 4.2 K. Solid lines—experimental curves, dashed lines—calculated curves. The matching is done at electric fields 0.005, 0.05, and 0.15 V/μm for samples RU001, RU002, and RU003, respectively. The dip at 37 μm is due to the GaAs reststrahlen band reflection.

The forward and reverse bias responsivity at low electric fields for sample RU002, having a 0.1 μm barrier layer thickness, is the lowest compared to the other two samples as shown in Figs. 7 and 8. This is due to the low optical electric field in the emitter. In accordance with the boundary conditions, tangential component of the electric field of the total incident and reflected waves must be zero at the surface of the highly conducting bottom contact. The electric field of the standing wave formed in the structure increases with the distance and has a maximum at a distance about a quarter wavelength from the bottom contact. Since the gap between the emitter and the highly doped bottom contact is the smallest for sample RU002, it has the lowest resultant optical electric field in the emitter. This leads to a very low photon absorption probability in accordance with Eq. (3), and therefore the loss in the responsivity.

This conclusion is confirmed by optical electric field calculations for these structures. The spectra of the normalized mean square optical electric field across the emitter and the bottom contact layers are shown in Fig. 9. The field for sample RU002 is the lowest compared to the others. This together with the lowest emitter concentration, leads to the lowest responsivity. The sharp drop at wavelength of 36.7 μm (where the permittivity drastically increases) is due to TO phonons. At the wavelength of LO phonons (33.9 μm) the permittivity is almost zero, creating a high electric field, which produces a responsivity peak in the experimental curves in Figs. 5 and 6. The first order resonance cavity peak

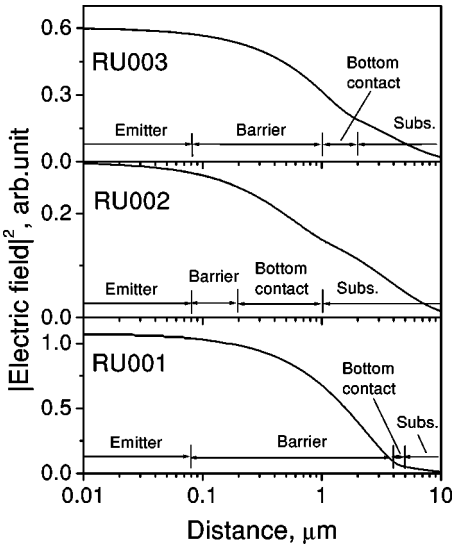

FIG. 10. Calculated optical electric field distribution of the standing wave generated in the samples at wavelength 34 μm. The maximum field is achieved at the surface. Low electric field for sample RU002 is due to the smallest barrier thickness compared to RU001 and RU003.

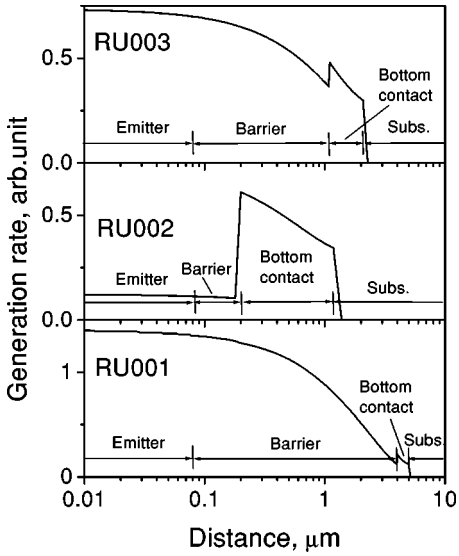

FIG. 11. Calculated generation rate across the structures at wavelength 34 μm. High generation rate in the emitter and the bottom contact is a result of high doping concentration. For the sample RU002 the generation rate in the emitter is lower compared to that in the bottom contact.

was seen at 68 μm for sample RU001. The second order peak for this sample and the first order peak for samples RU002 and RU003 are outside the measured spectral range, as indicated earlier. The small peak shift, towards the short wavelength from 33.9 μm, for sample RU001 is due to the contribution of the strong second order resonant cavity peak at around 23 μm. The optical electric field in the emitter is less than that in the bottom contact for all samples as seen in Fig. 9. The relative magnitude of the responsivity for forward and reverse directions (photogeneration of holes in the emitter and the bottom contact, respectively) depends on the relative values of the optical electric fields, thickness, and the hole scattering length.

The optical electric field distribution of the standing wave across the structures for 34 μm is shown in Fig. 10. The maximum intensity is obtained at the emitter surface and the field in the bottom contact is very low for all samples. Sample RU002 has a relatively low electric field inside the barrier and at the surface, resulting in the lowest responsivity. Since the skin depth corresponding to 34 μm is greater than the thickness of the emitter and the bottom contact, the sample would allow the radiation to penetrate into the substrate.

From Eq. (3), photon absorption probability in the layers depends not only on the electric field, but also on the imaginary part of the dielectric constant depending on the doping concentration. The distribution of generation rate, defined as the attenuation rate of η_a across the structure, for 34 μm radiation is shown in Fig. 11. Sample RU002 has the lowest generation rate in the emitter leading to the lowest responsivity. This is due to the weak optical electric field in the emitter and its low doping concentration. As shown in Fig. 11, in contrast to the emitter, the generation rate in the bottom contact is nonuniform, and this was taken into account for the responsivity calculation.

IV. CONCLUSION

In summary, HIWIP detectors with enhanced responsivity, low dark current, and remarkably high quantum efficiency have been observed. Even though all detectors are single emitter layer structures, the responsivity is greater than for the previously demonstrated multilayer structures. Responsivity and cutoff wavelength show a strong bias dependence. The main features of the absorption and responsivity spectra are well described by the model of free heavy/light hole absorption, photoemission, and hot carrier transport. Increased responsivity at range 40–60 μm is due to transitions from ground to excited states of the impurity.

ACKNOWLEDGMENTS

This work was supported in part by the NSF under Grant No. ECS-0140434. MBMR is supported by GSU RPE funds. The work at NRC is supported in part by DND. The authors thank T. Oogarah and K. Liu for samples preparation and S. Rolfe for SIMS measurement.

[1] M. W. Werner, Infrared Phys. Technol. **35**, 539 (1994).
[2] E. E. Haller, Infrared Phys. **35**, 127 (1994).
[3] D. M. Watson, M. T. Guptill, J. E. Huffman, T. N. Krabach, S. N. Raines, and S. Satyapal, J. Appl. Phys. **74**, 4199 (1993).
[4] J. E. Huffman, A. G. Crouse, B. L. Halleck, T. V. Downes, and T. L. Herter, J. Appl. Phys. **72**, 273 (1992).
[5] A. G. U. Perera, H. X. Yuan, and M. H. Francombe, J. Appl. Phys. **77**, 915 (1995).
[6] S. M. Sze, *Physics of Semiconductor Devices* (Wiley, New York, 1981).
[7] N. F. Mott, *Metal-Insulator Transitions* (Barnes and Noble, New York, 1974).
[8] A. G. U. Perera, H. X. Yuan, S. K. Gamage, W. Z. Shen, M. H. Francombe, H. C. Liu, M. Buchanan, and W. J. Schaff, J. Appl. Phys. **81**, 3316 (1997).
[9] A. G. U. Perera, S. G. Matsik, M. B. M. Rinzan, A. Weerasekara, M. Alevli, H. C. Liu, M. Buchanan, B. Zvonkov, and V. Gavrilenko, Infrared Phys. Technol. (in press).
[10] A. L. Korotkov, A. G. U. Perera, W. Z. Shen, J. Herfort, K. H. Ploog, W.

J. Schaff, and H. C. Liu, J. Appl. Phys. **89**, 3295 (2001).
[11] A. G. U. Perera, S. G. Matsik, M. Ershov, Y. W. Yi, H. C. Liu, M. Buchanan, and Z. R. Wasilewski, Physica E (Amsterdam) **7**, 130 (2000).
[12] G. M. Williams, R. E. DeWames, C. W. Farley, and R. J. Anderson, Appl. Phys. Lett. **60**, 1324 (1992).
[13] J. S. Blakemore, J. Appl. Phys. **53**, R123 (1982).
[14] S. Zangooie, M. Schubert, D. W. Thompson, and J. A. Woollam, Appl. Phys. Lett. **78**, 937 (2001).
[15] D. G. Esaev, S. G. Matsik, M. B. M. Rinzan, A. G. U. Perera, H. C. Liu, and M. Buchanan, J. Appl. Phys. **93**, 1879 (2003).
[16] R. F. Kirkman, R. A. Stradling, and P. J. Lin-Chung, J. Phys. C **11**, 419 (1978).
[17] N. O. Lipari and A. Baldereschi, Phys. Rev. Lett. **25**, 1660 (1970).
[18] W. Z. Shen, A. G. U. Perera, H. C. Liu, M. Buchanan, and W. J. Schaff, Appl. Phys. Lett. **71**, 2677 (1997).
[19] A. G. U. Perera, in *Handbook of Thin Film Devices Frontiers of Research, Technology and Applications, Vol. 2—Semiconductor Optics*, edited by M. H. Francombe, A. G. U. Perera and H. C. Liu (Academic, New York, 2000), pp. 135–169.
[20] M. Seon, M. Holtz, W. M. Duncan, and T. S. Kim, J. Appl. Phys. **85**, 7224 (1999).